Composite Structures 283 (2022) 115068

Contents lists available at ScienceDirect

Composite Structures

journal homepage: www.elsevier.com/locate/compstruct

Cyclic shear-compression testing of brick masonry walls repaired and retrofitted with basalt textile reinforced mortar

Larisa Garcia-Ramonda [a,*], Luca Pelà [a], Pere Roca [a], Guido Camata [b]

[a] Department of Civil and Environmental Engineering, Universitat Politècnica de Catalunya (UPC-BarcelonaTech), Jordi Girona 1-3, 08034 Barcelona, Spain
[b] Department of Engineering and Geology, University "G. D'Annunzio" of Chieti-Pescara, viale Pindaro 42, I-65127 Pescara, Italy

ARTICLE INFO

Keywords:
Cyclic shear compression test
Masonry
Textile Reinforced Mortar (TRM)
Fibre Reinforced Cementitious Matrix (FRCM)
Seismic strengthening
Ductility

ABSTRACT

This paper reports an experimental programme on masonry walls composed of handmade solid clay brick and hydraulic lime mortar. Reversed cyclic shear compression tests were carried out on the walls in three different configurations: unreinforced, repaired and retrofitted, and just retrofitted. Damaged walls were repaired and retrofitted with Basalt Textile Reinforced Mortar (B-TRM) and tested again to investigate the recovery of strength, stiffness and the improvement in drift capacity. The repair consisted in filling the open cracks and replacing the damaged bricks by following the so-called "scuci-cuci" technique. The just retrofitted configuration consisted of externally bonded B-TRM on undamaged walls. The B-TRM system comprised continuous bidirectional grids of basalt fibre embedded in hydraulic lime mortar on both surfaces of the walls. The experimental results showed the suitability of the proposed solutions for seismic retrofit and post-earthquake repair of existing masonry buildings. The research results highlighted the capacity of the proposed repair technique to reinforce damaged walls and the effectiveness of the investigated B-TRM system in increasing the resistance, the ductility, and the energy dissipation of unreinforced clay brick masonry. In addition, the results allowed a better understanding of the behaviour of masonry walls subjected to cyclic horizontal displacement in terms of failure mechanism and displacement capacities.

1. Introduction

Masonry is one of the oldest construction techniques used worldwide. Its profusely use lies not only on its ease of construction but also on its efficiency to withstand vertical gravitational loads. However, when masonry buildings are affected by horizontal loading, such as the earthquake action, they may show large vulnerability, as repeatedly observed in recent seismic events [1].

As one of the main historical construction materials, masonry is abundant in the built cultural heritage located in many earthquake-prone regions of the world. Therefore, the evaluation of their shear behaviour is absolutely essential. After recent seismic events, such as L'Aquila 2009 (Italy), Canterbury 2010 (New Zealand), Emilia 2012 and Amatrice-Norcia-Visso 2016 (Italy) earthquakes, composites materials for post-earthquake repair and seismic retrofitting of masonry structures have received a growing interest from the scientific community. To improve the poor structural performance of unreinforced masonry shear walls (URM) under seismic actions, different strengthening techniques have been developed.

Among the proposal of different strengthening techniques, Fibre Reinforced Polymers (FRP) reached worldwide consensus at the early stages of their development. FRP systems have been profusely utilized due to their high tensile strength, lightweight, relative ease of installation and resistance to corrosion. The research carried out on the use of FRP has shown its ability to successfully enhance the in-plane strength of masonry walls, as evidenced in [2–4]. However, FRP systems have shown meaningful limitations precluding their use in several cases. For instance, high or low temperatures might compromise the efficiency of FRP systems, and wet lay-up FRP applications are not possible either on moist surfaces or at low temperatures. In addition, FRP systems typically act as a vapour barrier and therefore, cannot be used when permeability is required, as in the case of existing masonry structures. These drawbacks stem mainly from the epoxy matrix, which acts both as the binder of the fibres and the bonding agent between the composite and the substrate.

The alternative solution to FRP systems consists in replacing the epoxy resins by inorganic matrices, among which the most common ones are lime-based or cement-based mortars. Textile reinforced mortar (TRM), also known as Fibre Reinforced Cementitious Matrix (FRCM), consisting of cement or lime mortar reinforced with different types of

* Corresponding author.
E-mail addresses: larisa.garcia.ramonda@upc.edu (L. Garcia-Ramonda), luca.pela@upc.edu (L. Pelà), pere.roca.fabregat@upc.edu (P. Roca), g.camata@unich.it (G. Camata).

https://doi.org/10.1016/j.compstruct.2021.115068
Received 28 June 2021; Received in revised form 26 October 2021; Accepted 4 December 2021
Available online 24 December 2021

fibres, has been receiving increased attention due to its mechanical efficiency and satisfactory compatibility with the masonry substrate, overcoming most of FRP's drawbacks.

An increasing research effort is now being undertaken to validate efficient masonry seismic strengthening techniques, based on TRM, to improve masonry's in-plane load-bearing and displacement capacity.

Experimental testing provides the fundamental approach for the understanding of the mechanical behaviour and failure of walls strengthened by means of TRM systems. The Diagonal Compression Test (DCT) and the Shear Compression Test (SCT) are the main test methods used in the study of the in-plane response of masonry walls. The effectiveness of TRM as a retrofitting technique has been successfully assessed on different masonry typologies by means of DCT [5–9]. DCT has shown to provide relevant results on the load bearing capacity. However, this type of test does not provide direct information on the deformation capacity, because the drift results are not representative of the real behaviour of the structure under seismic action. However, the accurate definition of damage levels, which can be quantified from experimental results, is of utmost importance when designing a repair or strengthening solution. As evidenced by [10], monotonic tests lead to larger drift capacities than cyclic ones. Therefore, cyclic SCT should be used to complement the experimental characterization in terms of displacement capacity. In addition, reversed cyclic SCT allows the determination of the force–displacement properties and hysteretic data of the structure, including the ductility capacity, secant stiffness, damping and energy dissipation.

There is a moderate amount of literature regarding the in-plane enhancement of Confined Masonry (CM) strengthened with TRM [11–13], stone masonry strengthened with TRM [14,15] and hollow concrete block masonry walls strengthened with Textile Reinforced Concrete (TRC) [16,17]. However, the available research on the behaviour of clay brick strengthened masonry is more limited [18,19]. The aforementioned experimental programmes focused on the characterization of different masonry typologies strengthened with TRM, comprising mainly carbon, glass and steel fibres, and limited research [20] focused on the study of vegetal fibre. Thus, research on the mechanical behaviour of masonry strengthened with basalt fibres (B-TRM) by means of SCT is missing. Different authors have already examined the excellent in-plane performance evidenced by clay brick masonry reinforced with B-TRM when tested in DCT [7–9].

After small or moderate seismic events, diagonal shear failure may be observed in in-plane horizontally-loaded masonry walls. In most cases the damage is superficially repaired and the structural member is covered by the reinforcement. Despite the strong need to assess the performance of the TRM retrofit of walls damaged by seismic actions, very limited experimental data are available. Both [9,21] performed DCT on repaired and retrofitted masonry walls with basalt bidirectional grid TRM embedded into lime-based mortar matrix (B-TRM). In the case of [21] no previous repairing intervention was performed prior to the B-TRM application and consequently the strengthened samples were not able to reach the peak load corresponding to the undamaged URM specimens. In [9] the damaged walls were repaired with a lime mortar repointing technique before the B-TRM application. In this case the walls showed a full recovery of their undamaged stiffness, as well as a significant enhancement of load capacity and ductility. These results highlight the importance of considering the influence of the damaged condition of the masonry substrate on the global behaviour of the strengthened wall.

Within this context, an experimental programme was designed to better understand the in-plane behaviour of clay brick masonry walls in three different configurations: unreinforced, repaired and retrofitted with B-TRM, and just retrofitted with B-TRM. The experimental programme consisted in executing reversed cyclic shear compression tests (SCT), on six specimens, in order to assess the efficiency of the TRM systems as post-earthquake repair and seismic retrofitting technique. In addition, one of the aims of the programme was to evaluate the in-plane structural behaviour of strengthened masonry walls in terms of lateral load-bearing capacity, displacement capacity, limit states, ductility, energy dissipation and damping coefficient. In order to evaluate the influence of the different configurations investigated (unreinforced, repaired and retrofitted) on the previously listed parameters, three variables were considered: condition of the substrate (damaged, undamaged), the presence of reinforcement (URM or retrofitted), and the failure mode experienced. Finally, the research aimed at identifying damage propagation and crack patterns in order to shed light on the failure mechanisms triggering the collapse of masonry walls on the three configurations investigated. This knowledge is of utmost importance for a better design of the different repairing and strengthening solutions.

2. Materials and specimens manufacturing

The experimental campaign was carried out at the Laboratory of Technology of Structures and Construction Materials (LATEM) at the Technical University of Catalonia (UPC-BarcelonaTech). This section presents the properties of the materials, the preparation of the specimens, their repairing and strengthening techniques, and the testing procedure.

2.1. Bricks and mortar

The masonry walls were built using handmade solid clay bricks fired with traditional procedures and lime-based mortar. The brick's mechanical properties were determined based on compression and flexural tests following the EN 772-1:2011 [22] and the EN 772-6:2001 [23]. The normalized compressive strength $f_{b,c}$ and the flexural strength $f_{b,f}$ of the bricks were equal to 17.99 MPa (C.o.V 8.30%) and 2.44 MPa (C.o.V 20.0%).

The mortar used to bind the units was derived from a hydraulic lime-based commercial premix by reducing its compressive strength with limestone filler addition in order to replicate a low strength historical lime mortar [24]. Following the EN 1015-11:1999 [25], prismatic samples with dimensions 160 × 40 × 40 mm^3 were prepared during the construction of each wall, to evaluate the strength of the mortar. The flexural strength $f_{m,f}$ was evaluated on nine prismatic specimens for each wall built, while the compressive strength $f_{m,c}$ was assessed on the eighteen halves produced by the splitting of the samples under flexure. The flexural and compressive strength yielded values equal to 0.57 MPa (C.o.V 22.50%) and 2.58 MPa (21.60%), respectively.

The compressive strength of the masonry was studied by [26]. The obtained average strength was 6.50 MPa (C.O.V 9%).

2.2. Textile reinforced mortar

For the retrofitting of the masonry walls a Basalt Textile Reinforced Mortar (B-TRM) solution was symmetrically applied on the specimens. The textile consisted in a bidirectional grid of low-density basalt (LDB) fibres with steel micro-cords and 17 × 17 mm^2 grid spacing. Table 1 reports the relevant properties of the textile, as provided by the manufacturer and some specific studies [27–29].

The mortar matrix used for the application of the textile fabric was a premixed NHL 3.5 natural hydraulic lime. Following the EN 1015-11:1999 [25], prismatic samples were cast into metallic moulds with dimensions 160 × 40 × 40 mm^3 after the preparation of every batches of mortar to evaluate the strength of the mortar in each retrofitted wall. The flexural strength $f_{rm,f}$ was evaluated on six prismatic specimens for each wall built, while the compressive strength $f_{rm,c}$ was assessed on the twelve halves produced by the splitting of the samples under flexure. The flexural and compressive strength yielded the values equal to 3.51 MPa (C.o.V 8.10%) and 12.95 MPa (7.90%), respectively. The Young's modulus of the mortar matrix, $E_{rm,st}$ is 9 GPa as provided by the manufacturer.

Table 1
Mechanical properties of the textile used for the reinforcement of the walls as provided by the manufacturer and some specific studies [27].

Product	Young's modulus[a]	Ultimate Tensile Strength[a]	Strain at failure[a]	Thickness[a]	Tensile capacity from shear bond test [27]
	E [GPa]	$\sigma_{u,f}$ [MPa]	$\varepsilon_{u,f}$	t_f [mm]	$\sigma_{sl,t}$ [MPa]
LDB	90	1700	0.019	0.032	1049

[a]Provided by the manufacturer.

A good mortar-textile interlocking leads to a good exploitation of the tensile strength of the textile $\sigma_{u,f}$, precluding a failure mode involving the reinforcement-substrate interface. To assure that such failure mode does not occur, a proper effective bonded length L_{eff} of the composite on the substrate has to be provided. L_{eff} represents the minimum length needed to fully allow the shear stress transfer from the substrate to the TRM strengthening system so the textile can carry all the tensile stress. The shear bond test allows the identification of L_{eff} and the assessment of the tensile capacity, $\sigma_{sl,t}$, of the B-TRM. Different experimental programmes [28–31] investigated the performance of 21 B-TRM specimens, using three different bonded lengths equal to 220, 260 and 345 mm, subjected to single lap shear bond test. The results evidenced that failure due to fibre rupture of the basalt was the most common failure mode. Consequently, it could be concluded that the effective bonded length for this type of TRM composite is lesser or equal to 220 mm. The tensile stress of the reinforcement $\sigma_{sl,t}$ attained by each specimen was derived as the peak load divided by the cross section area of the dry textile. Table 1 shows the average value of $\sigma_{sl,t}$ yielded from the results of the aforementioned researches.

2.3. Construction, repair and strengthening

Four double leaf masonry walls with nominal dimensions 1270 × 1270 × 310 mm^3 were built in the laboratory by professional personnel. The construction process of the specimens considered the procedure shown in Fig. 1. The specimens were built in Flemish bond with 21 courses and 15 mm thick mortar joints. Finally, a concrete beam was cast on top of the specimens to allocate the set-up device in charge of applying the reversed horizontal displacement. The finished walls were stored under laboratory conditions during the 28 days required for the curing of the mortar.

2.3.1. Strengthening

The specimens were strengthened twenty-eight days after their construction by professional workers from the manufacturer company. From the four specimens built, two were left unreinforced. These URM specimens were tested, and as a result two damaged specimens were later repaired and retrofitted with Basalt Textile Reinforced Mortar (B-TRM), as described in the following subsection. The remaining two specimens were retrofitted with B-TRM strengthening systems following the procedure show in Fig. 2.

To implement the strengthening, the surfaces of the walls were prepared by removing the dust and by creating grooves along the vertical and horizontal mortar joints to generate the necessary grip between the surface of the wall and the mortar matrix of the TRM. The specimens were wet with abundant water to prevent masonry from absorbing the water during the application of the TRM. First, a thin layer of mortar matrix was applied on the surface of the specimen. Then the textile was embedded in the matrix by applying a light pressure to guarantee the right adherence to the support and to fill all the voids of the mesh. Two basalt sheets, of 800 mm width each, were applied on each side of the wall with an overlap of 300 mm in the centre of the panel. The length of the overlapping was based on the previous analysis performed on the bonded length results obtained by [28,32] and was designed to guarantee a satisfactory stress transfer between the surface of the wall and the TRM. The second layer of mortar matrix was applied to cover the basalt grid. The final thickness of the TRM reinforcement varied between 8 to 10 mm. This procedure was repeated on both surfaces of the specimens. Once the hardening of the mortar had begun, the faces were wet to favour the curing and then were wrapped with sackcloth fabric, which was kept wet for the following 7 days and wrapped with plastic sheets to preserve the humidity of the specimens.

2.3.2. Scuci-cuci repairing technique

The two unreinforced specimens were tested under SCT. Since the specimens evidenced apparent damage after testing, they were re-paired using a combination of the *Scuci-cuci* technique and lime mortar repointing, as shown in Fig. 3.

The aim of the repair was to restore the wall's structural continuity along the cracks and to recover its initial stiffness, lost at the end of the test. The restoration was achieved by substituting the fractured units, located in the corners and central part of the wall, with new ones and recovering the locally heavily damaged parts of the masonry. The material used for the restoration was the same one used for the construction in order to assure a good compatibility in terms of stiffness and resistances, which is key to a good collaboration among new and existing elements. The cracks of the specimens observed in the final crack pattern were opened using a rotary hammerdrill accessorized with a 20 mm width flat chisel, and a hand tool 30 mm width flat chisel. The fractured bricks were replaced by new ones. Afterwards, the cracks were filled with the same lime-based mortar used for the retrofitting of the walls.

3. Experimental programme

To investigate the performance, and the efficiency, of B-TRM as post-earthquake repair and seismic retrofitting technique, a reversed cyclic shear compression test was designed following the standard FEMA 461 [33]. From the response of the specimens it is possible to evaluate key parameters such as the effective stiffness K_e, the dissipated energy E_d, and the equivalent viscous damping ξ_{eq}. These parameters are of interest to evaluate the seismic performance of masonry buildings. In addition, pseudo-static cyclic loading tests are used to study the hysteretic behaviour and degradation of strength and stiffness under repeated loading.

3.1. Set-up

Fig. 4 includes a general view of the experimental set-up to performed the reversed cyclic shear compression test. During construction, the samples were laid on a metallic C-profile filled with concrete which, during the test, allowed the sliding shear failure to potentially occur in the bed joints of the first course of bricks. In addition, the base was constrained at both ends by two T-shape devices. Both the base and the end-devices were fixed to the strong floor of the laboratory by means of post-tensioned steel bars. On top of the wall a reinforced concrete (RC) beam was placed. This element had the double function of allowing the smooth distribution of the vertical load and allocating the plates receiving the horizontal cyclic loading by the actuator. On the top of the RC beam laid a stiff metallic H profile stiffened with ribs, where the vertical load was applied with two jacks of 1000 kN capacity each. The jacks reacted against a stiff frame anchored to the strong floor. Between the RC beam and metallic profile, a 3 mm thick Teflon sheet and a 3 mm thick PVC sheet were inserted to provide a smooth horizontal surface and avoid the shear deformation of the vertical jack caused by

Fig. 1. Construction procedure: (a) placing of the rulers for the construction, (b–c) construction of the wall in Flemish bond, (d) rebars placing for the concrete beam located on top of the specimen, (e) cast of the concrete beam, (f) specimen finished and stored under laboratory conditions.

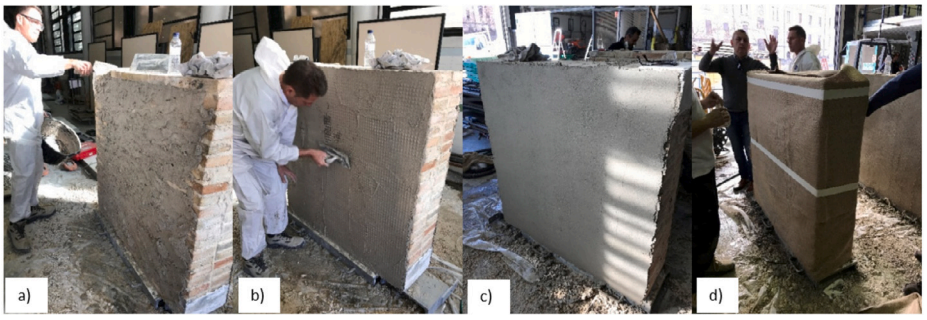

Fig. 2. Procedure for the application of the B-TRM strengthening system: (a) application of the first layer of mortar, (b) set of the basalt grid, (c) finished look of the wall retrofitted with B-TRM, (d) wrapping of the specimens with wet sackcloth fabric for curing.

Fig. 3. *Scuci-cuci* intervention: (a) Removing of fractured units, (b) replacing of fractured units, (c) cracks opening with a hand tool, (d) filling of cracks with lime based strengthening mortar.

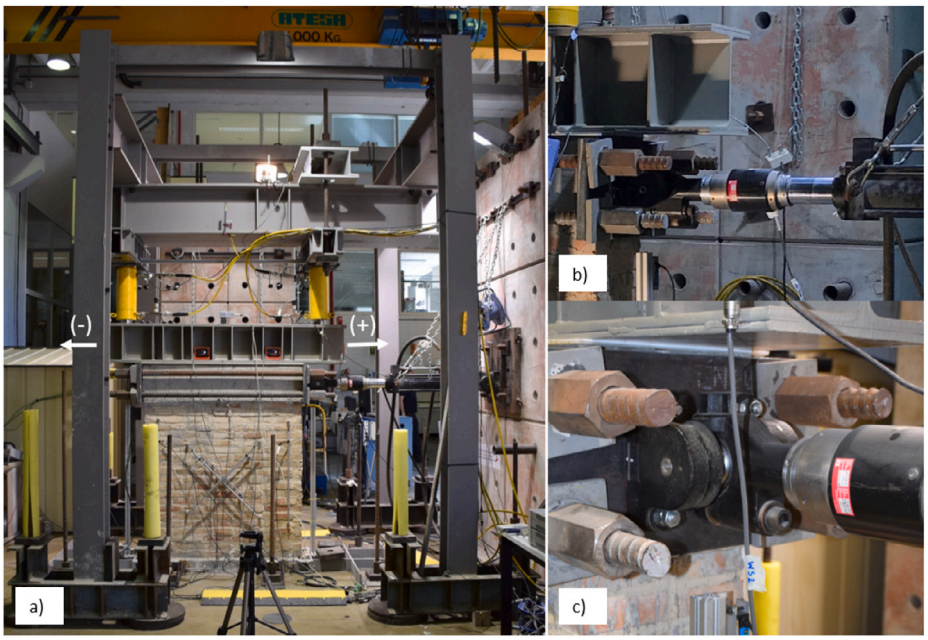

Fig. 4. (a) General view of the Shear Compression Test set-up, (b) detail of the plate and rods mounted aligned with the actuator to applied the loading protocol, (c) hinged connection that allowed the reversed cyclic loading.

the friction generated by the horizontal loading of the wall. Between the RC beam and the PVC sheet a layer of cement-based mortar, with thickness of 5 to 10 mm, was inserted in order to level the end surface of the beam and guarantee the vertical load transfer avoiding stress concentration due to irregularities.

The shear compression tests were performed in two steps. Firstly, the vertical force V was gradually applied under force control. The valves of the jacks were closed once the designed compression stress was reached. Such compression stress was taken equal to σ_v=0.3 MPa, which corresponds to the typical vertical load for a two-storey masonry building. Secondly, the imposed horizontal displacement was applied with a hydraulic actuator anchored to a reaction wall. The actuator had a full stroke of 500 mm and a pushing and pulling capacity of 350 kN and 250 kN respectively. Two steel plates (530 × 300 × 30 mm^3) connected by 4 steel rods of 40 mm diameter were mounted aligned with the horizontal actuator. One of the plates was connected to the horizontal actuator by means of a hinge, enabling the application of reversed cyclic loading in the horizontal direction, as shown in Fig. 4. With the valves of the actuators closed, no vertical displacement or rotation of the top of the wall was possible at this stage, and applying horizontal load induced a double bending condition [34]. As a consequence of the testing mode, the vertical load increased together with the horizontal load generated by the imposed displacement. This increment of the vertical load was measured by means of four pressure transducers located one on each oil chamber of the two double effect vertical jacks. These sensors allowed us not only to control the vertical load variation but also to know its distribution throughout the cyclic test.

A combination of instruments was placed on both specimens' faces in order to capture their in-plane response. In total, ten linear variable displacement transducers (LVDT) with a displacement range of +/- 5 mm and a precision of 5 μm, eight potentiometer displacement transducers, two laser sensors, two wire sensors, one inclinometer and four pressure transducer were installed for each test. Among the LVDTs, four were mounted to measure the specimens' diagonal displacements and control the cracking of masonry and the deformation of the basalt textile.

3.2. Cyclic loading test

As aforementioned, the loading protocol was designed following FEMA 461 [33]. The quasi-static cyclic testing protocol replicates the seismic effects by the slow application of cyclic displacements. The adopted approach aimed to identify and capture accumulated damage, to enable the detection of the failure mechanism and to determine the force–displacement properties. The loading history consisted of repeated cycles of step-wise increasing deformation amplitudes. Three cycles at each displacement amplitude were completed. In a complete cycle the target displacement was imposed in the positive and negative loading direction, returning to the original position of the wall. The loading history adopted for all the SCT test is shown in Fig. 5. The loading protocol included 29 displacement amplitude steps and a total number of 87 cycles.

4. Analysis of results and discussion

This section presents the results of the experimental campaign for each type of specimens tested. The response of the specimens is presented in terms of cracking patterns and experimental force–displacement curves. Table 2 shows the values of the most relevant parameters for the positive and negative direction for each specimen tested. The following subsections describe the response experimentally observed grouped according to the specimens' configurations: unreinforced, repaired and retrofitted, and just retrofitted. The values of the parameters analysed, such as displacements, in each case are obtained as the average values of the two specimens tested with the same configuration.

4.1. Type of failure

Fig. 6 shows the crack pattern at the end of the test of all the specimens. The final damage of the URM walls was characterized by a diagonal stair-stepped cracking mainly developed through the mortar joints and by tensile splitting of some units. With increasing displacement amplitudes, the cracks developed until a wide crack formed along each diagonal leading to global failure. For both URM specimens the

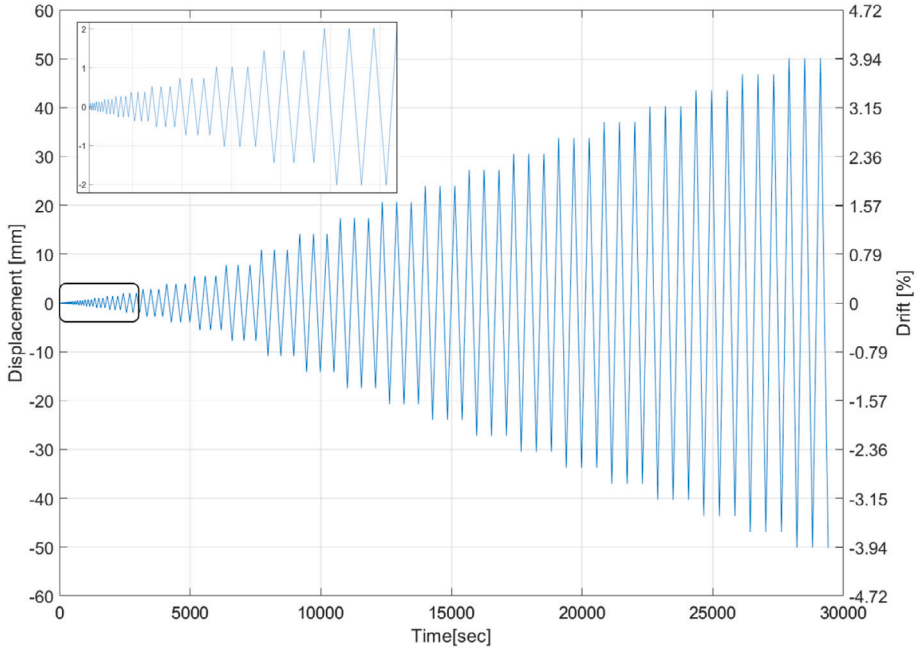

Fig. 5. Loading history for the shear compression testing of the specimens.

Table 2
Summary of the main results. Brackets show the values in [push, pull] directions.

Properties	URM_1	URM_2	URM1_R	URM2_R	LDB_1	LDB_2
Displ. at cracking [mm]	[−5.6, 5.6]	[−5.6, 5.5]	[−4.1, 6.3]	[−5.6, 7.8]	[−5.6, 7.8]	[−4.1, 4.0]
Displ. at yielding [mm]	[−8.5, 8.5]	[−8.4, 7.7]	[−5.5, 8.7]	[−7.2, 9.6]	[−8.1, 10.8]	[−5.9, 5.8]
Displ. at peak load [mm]	[−10.9, 10.9]	[−10.9, 10.9]	[−14.3, 14.3]	[−14.3, 14.2]	[−14.2, 14.2]	[−11.0, 10.9]
Ultimate displ. [mm]	[−14.2, 14.2]	[−13.9, 12.3]	[−16.0, 17.1]	[−21.7, 17.9]	[−17.9, 19.1]	[−14.9, 13.2]
Ductility	1.66	1.63	2.45	2.44	1.99	2.4
Cracking load [kN]	[−114.5, 114]	[−102.3, 105.0]	[−120.7, 126.1]	[−142.2, 132.4]	[−135.8, 146.2]	[−152.5, 122.1]
Peak load [kN]	[−192.4, 150.7]	[−162.9, 151.6]	[−175.1, 180.1]	[−194.6, 167.9]	[−213.1, 207.2]	[−244.7, 196.7]
Ultimate load [kN]	[−176.0, 176.0]	[−154.2, 146.4]	[−161.5, 174.4]	[−182.0, 162.9]	[−195.9, 202.8]	[−221.4, 175.3]
H_{cr}/H_{max}	0.59	0.66	0.7	0.76	0.68	0.62
$K_{initial}$ [kN/mm]	28	35	44	36	35	53
K_e [kN/mm]	21	19	25	21	21	34
$K_e/K_{initial}$	0.75	0.54	0.57	0.58	0.6	0.64

first cracks were visible, in the pushing direction, at the centre of the panel at a displacement equal to δ_{cr} = 5.5 mm (drift θ_{cr}= 0.4%). Shortly after the concentration of cracks on each diagonal, the maximum load was attained at a displacement $\delta_{H_{max}}$= 10.9 mm (drift $\theta_{H_{max}}$= 0.9%). Specimen URM_1 only showed one diagonal crack because the test was not continued after the development of this crack. After the peak load, the degradation of the specimens was sudden and characterized by the shearing of the corners and crushing of the bricks.

The repaired and retrofitted specimens (URM_R) also showed diagonal cracks with severe damage occurring in the region where the two cracks intersected. After the onset of cracking, the width of the existing cracks increased at each following displacement amplitude, enlarging the damage. Despite the repair, the URM_R specimens evidenced their first visible crack in an early stage at a displacement equal to δ_{cr}= 4.00 mm (drift θ_{cr}= 0.3%), when compared to the URM. These first cracks appeared in the pushing direction, while in the pulling direction the cracks were visible in the following amplitude step. The maximum load was attained at a displacement $\delta_{H_{max}}$= 14.3 mm (drift $\theta_{H_{max}}$= 1.1%) in both directions and for both specimens. The cracks re-opening of the damaged specimens led to an early stress transfer from the masonry to the LDB grid causing the spalling of the mortar and forcing the LDB grid to withstand more displacement cycles. For this reason the URM_R specimens showed a more diffuse crack pattern at the centre of the panel, when compared to LDB specimens, see Fig. 6 - *b,c*. In addition to the re-opening of the repaired cracks, and as a result of the stress redistribution provided by the TRM strengthening system, additional cracks took place on both diagonals. Finally, the global failure of both specimens was due to tensile diagonal cracking on both directions. After the peak load was attained and in the softening branch of the experimental curve, the TRM failed due to tensile fracture because of the attainment of its tensile strength. The attainment of this stress state was confirmed by the LVDT recordings.

The specimens just retrofitted with B-TRM (LDB) presented a rather heterogeneous response when compared with the repaired ones (URM_R). Specimen LDB_1 showed its first visible cracks at displacement equal to δ_{cr}= 6.71 mm (drift θ_{cr}= 0.5%), while specimen LDB_2 presented an early cracking at a displacement equal to δ_{cr}= 4.05 mm (θ_{cr}= 0.3%). The difference in the response between the LDB specimens can be attributed to the different failure mechanisms experienced by them. Specimen LDB_2 showed a mixed mechanism combining diagonal tensile cracking and frictional sliding along two central bed joints, while specimen LDB_1 showed the tensile diagonal cracking failure seen in the URM and URM_R specimens. This difference also influenced the peak load. As in specimens URM_R, specimen LDB_1 attained its peak load at displacement of about $\delta_{H_{max}}$= 14.3 mm (drift $\theta_{H_{max}}$= 1.1%) in both directions. Specimen LDB_2, on the other hand, attained its peak load on an early stage at displacement $\delta_{H_{max}}$= 10.9 mm (drift $\theta_{H_{max}}$= 0.9%) in both directions.

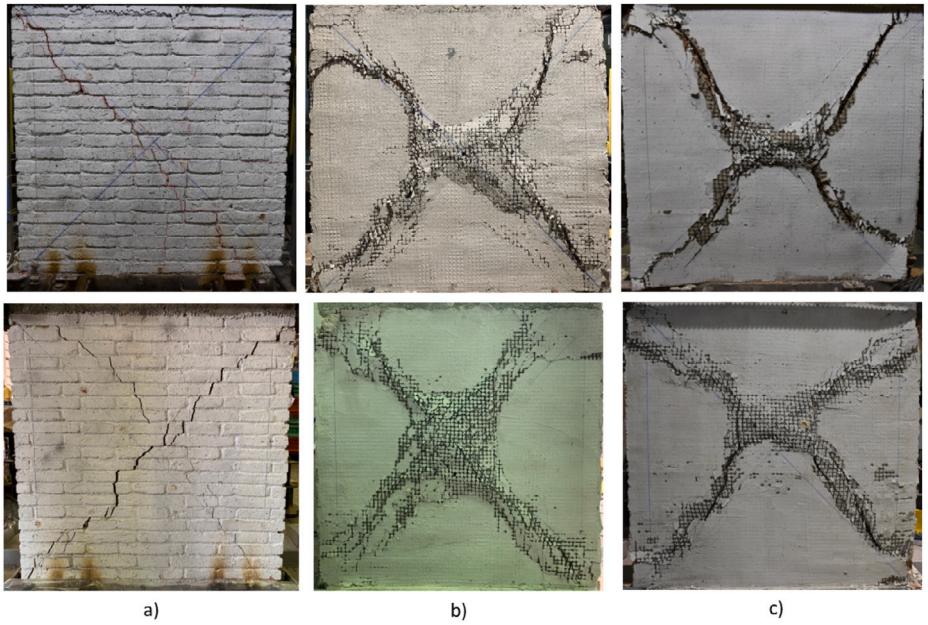

Fig. 6. Crack pattern at the end of the tests: (a) URM_1 (*up*) and URM_2 (*down*), (b) URM1_R (*up*) and URM2_R (*down*), (c) LDB_1 (*up*) and LDB_2 (*down*).

Despite the aforementioned particular features, all the specimens retrofitted with B-TRM (URM_R and LDB) evidenced a rather homogeneous response in terms of lateral deformation capacity. The enhancement provided by the reinforcement is appreciated at the displacement corresponding to the attainment of the maximum load. No toe crushing in compression was observed in any of the specimens during the test and up to the largest displacement amplitude attained.

4.2. Hysteretic response

Fig. 7 shows the experimental force–displacement curves under cyclic in-plane loading of all the specimens tested, together with their envelope curves. The envelope curves were derived from the experimental hysteretic curves and constructed by connecting the peak force at the first cycle of each displacement amplitude. The positive direction is the direction in which the horizontal hydraulic actuator pulls the specimen whereas the negative one is the direction in which the actuator pushes the specimen (Fig. 4). The displacement was measured at the top of the wall. The corresponding drift represents the lateral displacement over the total height of the specimen, expressed as a percentage.

In general, all the experimental curves were characterised by an initial linear branch corresponding to the undamaged behaviour of the structure. At the onset of cracking, and with the development of damage and energy dissipation, the response became non-linear, as evidenced by the force–displacement envelopes, while at the same time wider hysteretic loops were observed. The hysteretic loops widen progressively as the residual strength decreased until failure. According to [35], this behaviour can be associated to a typical shear failure mechanism, which is in agreement with the failure mechanism underwent by most of the specimens tested.

Among the unreinforced specimens, the attainment of the peak load was followed by the sudden brittle failure due to masonry's very limited tensile strength, as shown in Fig. 7 *a–b*. Given the brittleness of the response, the walls were unable to withstand inelastic deformation once the maximum lateral force was attained. The evolution of the damage can be related with the width of the hysteretic loops at increasing displacement amplitude. The wider the loop, the larger the damage experienced by the specimen. URM_2 evidenced wider hysteretic loops (see Fig. 7-*b*) which is in correspondence with the more severe damage observed during and after the test, see Fig. 6-*a*. Table 2 summarizes the main results of SCT. The load capacity of the URM specimens shows significant difference, mainly in the pushing direction. However, such difference can be fully explained by the inherent variability of the material constituents.

As aforementioned, and as a consequence of the early crack reopening observed on the repaired and retrofitted specimens, the improvement in lateral load-bearing capacity provided by the B-TRM was moderate. On average the enhancement was of only 10%, when compared with the URM walls. This demonstrates the influence of the substrate's damaged condition on the response of the B-TRM. However, the peak load was reached at a larger displacement compared with the URM walls, showing an increment of 31%. Consequently, the specimens' global behaviour showed larger deformation capacity and ductility compared to the URM specimens, as seen in Fig. 7 *c–d*. The experimental response shows that specimen URM2_R exhibited a more ductile and progressive damage than its pair URM1_R. This ductile behaviour, mainly observed on the post-peak, was achieved through energy dissipation translated into larger and wider hysteretic loops, while being able to withstand damage at higher values of lateral force, before the strength degradation took place. Both specimen showed a symmetrical force–displacement response in both directions, as seen in Fig. 7 and Table 2.

The just retrofitted specimens (LDB) showed a significant increment in both lateral-load bearing and deformation capacity of 31% and 30%, respectively. Such improvement validates the effectiveness of the reinforcement system, and once again shows the influence of the substrate condition on the load bearing capacity. As explained in the previous section, the LDB specimens experienced different failure mechanisms. This difference can be also seen in the experimental curves (Fig. 7 *e–f*). Specimen LDB_1 had a symmetrical response while LDB_2 showed a rather asymmetrical attainment of the peak load, as also seen in Table 2. The lateral capacity measured in the negative direction (pushing) was about 7% larger than that in the positive direction (pulling). In addition, specimen LDB_2 showed a rapid strength degradation after the peak load.

From the results of Table 2, it is evident that B-TRM reinforcement enhanced not only the global in-plane shear behaviour of the specimens but it also homogenized their structural response, mainly up to the attainment of the peak load, reducing the influence of the scattering of the mechanical properties of the masonry constituents.

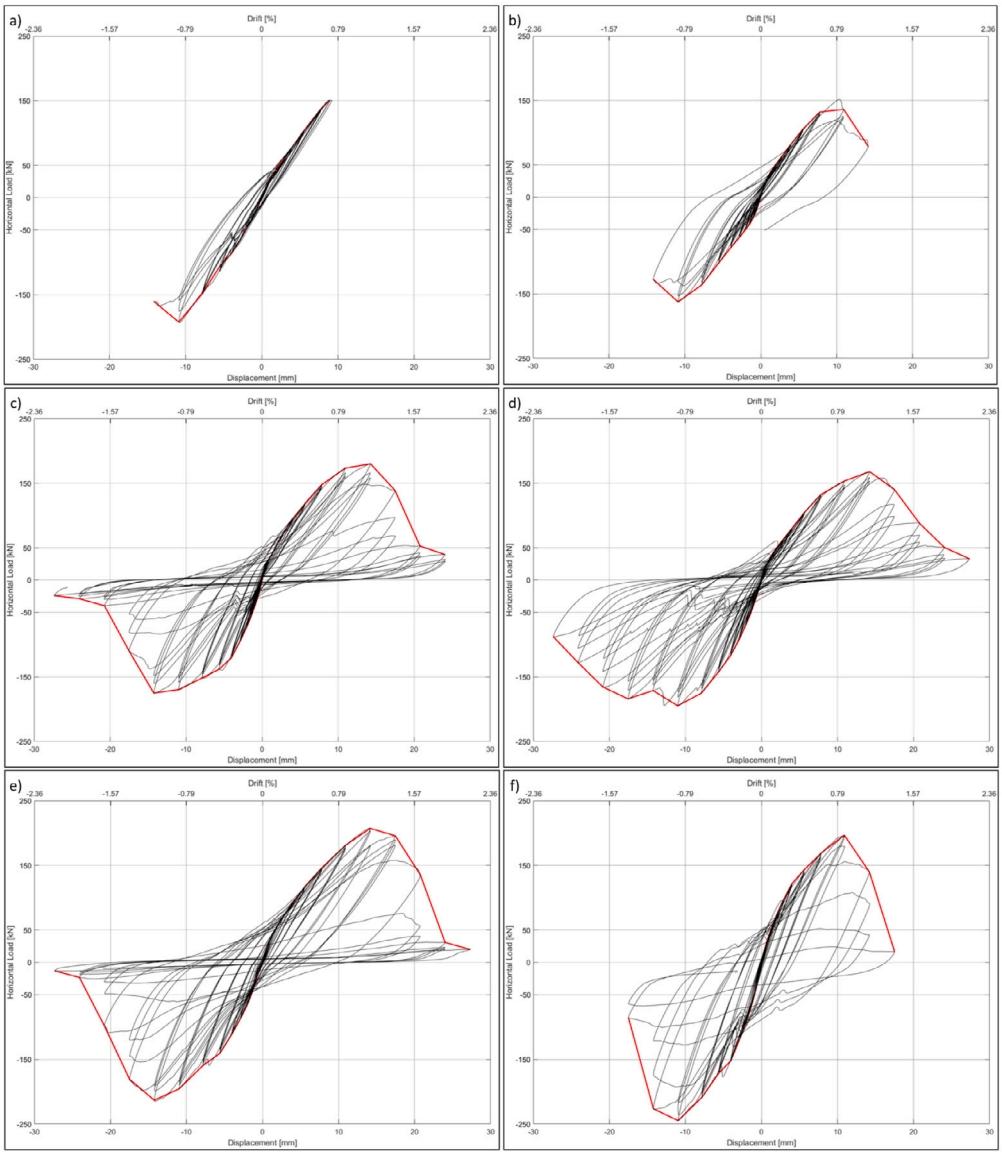

Fig. 7. Force–displacement hysteresis curves and envelope curves of tested walls: (a) URM_1, (b) URM_2, (c) walls repaired and retrofitted with B-TRM URM1_R and (d) URM2_R, (e) walls retrofitted with B-TRM LDB_1 and (f) LDB_2.

4.3. Bilinear idealization and ductility factor

The bilinear idealization proposed by [35] enables a reliable computation of the ultimate displacement δ_u, the ductility μ, and the effective stiffness K_e as proposed by [36]. The bilinear approximation of the experimental envelope curves was obtained as described in Fig. 8-*a*. First, the cracking point (δ_{cr}, H_{cr}) was identified. The cracking point corresponds to the moment at which the first cracks become visible and coincides with the change of slope in the envelope curve. The point corresponding to the peak load ($\delta_{H_{max}}$, H_{max}) was also identified. The ultimate displacement δ_u was determined as the displacement at which the lateral strength had dropped to 80% H_{max}. If such a large drop was not attained, the largest displacement reached during the test was taken as δ_u. The ultimate strength H_u is defined as the maximum load of the bilinear idealization and is determined so as to produce a bilinear curve enveloping the same area as the experimental envelope curve up to δ_u. The yielding displacement δ_y, which is the displacement at the idealized elastic limit, is then defined as the ratio between the ultimate strength H_u and the effective stiffness K_e. Fig. 8-*a* also shows the three limit states proposed by the Italian standard CNR-DT 212/2013 [37]. These limit states correspond to the damage limit state (DL3), significant damage limit state (DL4), and collapse limit state (DL5), which can be correlated with the points previously described for the bilinear idealization.

For the present application, the bilinear idealization was calculated for both positive and negative directions, except for specimen URM_1 for which it was performed for the negative direction and mirrored. Fig. 8-*b* shows the bilinear models corresponding to all specimens tested.

The ductility factor μ of each specimen is computed as the ratio between the ultimate displacement δ and the yielding displacement δ_y, following Eq. (1).

$$\mu = \frac{\delta_u}{\delta_y} \tag{1}$$

Table 2 shows the ductility obtained for each specimen tested. As mentioned in the previous section, URM specimens were characterised by a sudden and brittle failure. The application of B-TRM provided the masonry walls with larger capacity to sustain imposed displacements. On average, the increment in ductility of the specimens repaired and retrofitted with B-TRM (URM_R), and just retrofitted with B-TRM (LDB) was of 49% and 34% respectively.

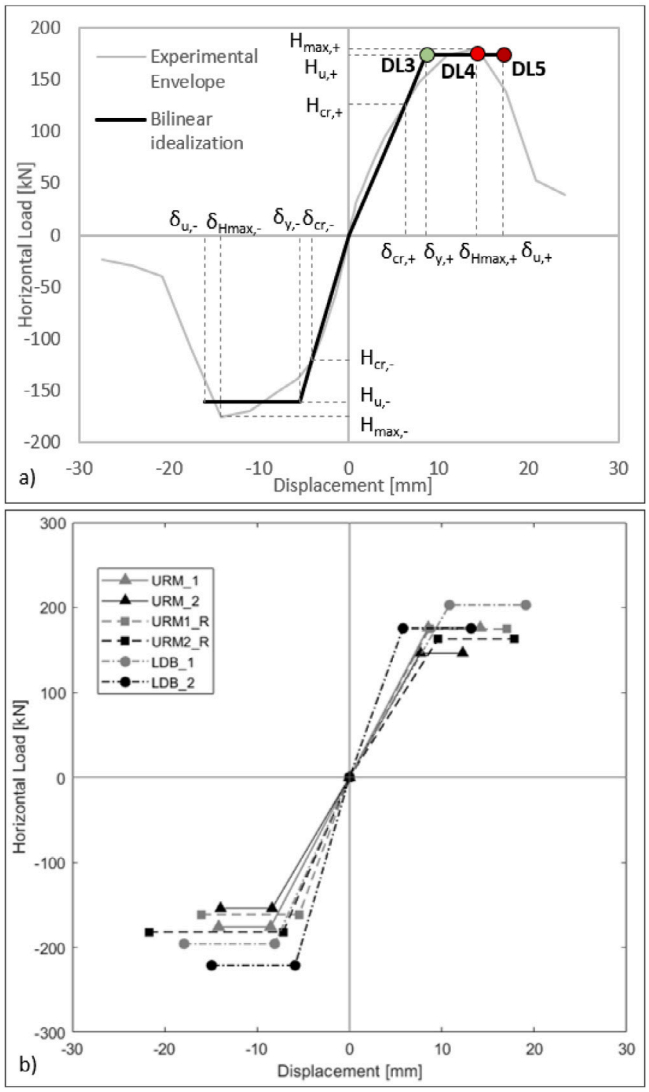

Fig. 8. Bilinear idealization: (a) Construction of bilinear response, (b) comparison between specimens tested.

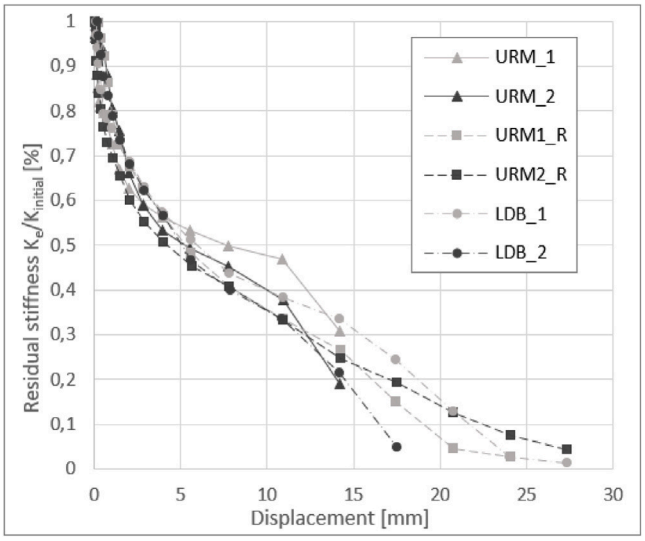

Fig. 9. Degradation of the lateral stiffness experienced by the specimens tested on SCT with increasing lateral displacement.

4.4. Secant stiffness and stiffness degradation

The effective stiffness K_e is defined as the secant stiffness to the experimental envelope curve at the onset of cracking [35]. The secant stiffness can be calculated as the ratio of the load at crack formation to its associated displacement, H_{cr}/δ_{cr}. Some authors such as [10,15,38] have also proposed the computation of the initial stiffness $K_{initial}$. This parameter is defined as the secant stiffness at 15% H_{max} of the experimental envelope curve, and can be considered as the stiffness of the uncracked section of the specimen. Both stiffnesses, computed for both the positive and negative branches of the experimental envelope curves and averaged, are shown in Table 2.

As can be seen in Fig. 8-*b* the initial stiffness is marginally affected by the reinforcement. This can be explained as due to the small thickness of the strengthening layers applied on the walls. The repaired and retrofitted specimens recovered the stiffness of the URM walls, which confirms the effectiveness of the repair treatment. In the case of the just retrofitted specimens, LDB_1 did not show any significant stiffness increment, while LDB_2 showed a 30% increment with respect to the URM cases.

Due to the complexity of the damage mechanisms experienced by the wall specimens, the degree of damage is not always easy to define. According to [17], a first approach to quantify the damage experienced by the walls consists of computing the stiffness degradation during the cycles. For that purpose, the lateral stiffness at each level of lateral displacement has been computed at the first cycle of each amplitude of the in-plane loading protocol. The stiffness at each level of displacement has been calculated as the secant stiffness at the peak force of each cycle considering positive and negative directions, as proposed by [39], following Eq. (2).

$$K_{e_i} = \frac{H_i^+ - H_i^-}{\delta_i^+ - \delta_i^-} \tag{2}$$

Where H_i^+ and H_i^- are the maximum forces in the positive and negative directions, respectively, for cycle i with their corresponding displacements δ_i^+ and δ_i^-.

As expected, the secant stiffness decreases as the lateral displacement increases. Fig. 9 shows the residual lateral stiffness, calculated as the percentage to the initial stiffness $K_{initial}$ with increasing displacement. During the uncracked phase of the test, there was a significant degradation of the initial stiffness even though the visual inspection did not reveal visible cracks. This can be explained by the internal microcracking formation in the mortar–brick interface, neither visible to the naked eye nor possible to be recorded by the applied instrumentation. At the moment of cracking (displacement δ_{cr}), the effective stiffness K_e had dropped to 50% of $K_{initial}$. This finding is of interest since the EC8 [40] recommends the use of the cracked stiffness when assessing the behaviour of masonry buildings under seismic actions. According to the standard, such stiffness should be taken as one-half of its respective uncracked value (i.e. the initial stiffness $K_{initial}$). The recommendation is made for unreinforced masonry and there are no guidelines when it comes to retrofitted masonry. However, the specimens retrofitted with B-TRM systems showed a good agreement with the EC8's recommendations, as shown in Table 2. The average value of the ratio $K_e/K_{initial}$ experimentally obtained is equal to 0.61 (C.o.V = 12.08%).

4.5. Energy dissipation

The energy dissipation capacity is an important parameter in the assessment of the seismic behaviour of masonry structures.

According to [39] the amount of dissipated energy E_d was calculated for the first cycle of each displacement amplitude. For the corresponding cycle the dissipated energy was calculated as the area

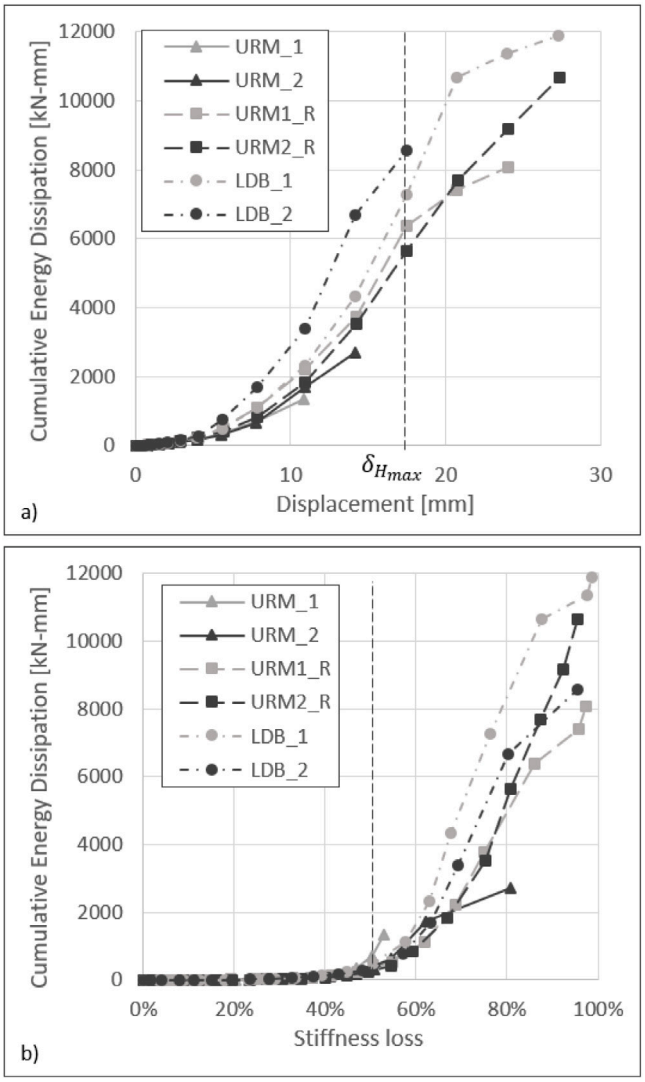

Fig. 10. Energy dissipation: (a) Cumulative energy dissipation vs. displacement, (b) Cumulative energy dissipation vs. stiffness loss.

within the hysteretic loop. The calculation was only done for completed cycles.

Fig. 10-*a* shows the cumulative energy dissipation E_D for all the specimens tested. In general terms, all the tested specimens exhibited a similar trend, showing increasing energy dissipation capacity with increasing displacement. As expected, all the specimens retrofitted with B-TRM (URM_R,LDB) showed higher dissipation capacity than the URM walls. The combination of repairing techniques and B-TRM application provided the URM_R specimens with the ability to dissipate more energy by reaching greater displacement amplitudes in the inelastic domain. On average, these specimens increased their energy dissipation capacity by 364%. The specimens just retrofitted with B-TRM (LDB) showed even higher dissipation capacity with average increase of the total energy dissipated equal to 406%. Such increment can be attributed to the action of the TRM after the cracking of the masonry. From Fig. 10-*a* it can be observed that the damaged condition of the masonry substrate on specimens URM_R only influenced their dissipation capacity after the peak load. In this figure, the average value of $\delta_{H_{max}}$ is marked with a dashed line. Beyond the peak load, the energy dissipation capacity of walls URM_R decreases significantly when compared with specimens LDB, in which the B-TRM was bonded on undamaged substrate.

Fig. 10-*a* also shows the influence of the failure mode on the energy dissipation capacity. The specimens failing due to diagonal tensile failure (URM, URM_R and LDB_1) showed similar values of energy dissipation for the same displacement amplitudes, while the only specimen (LDB_2) failing due to shear sliding showed always higher dissipation capacity for these same displacement amplitudes and up to the failure of the specimen.

Fig. 10-*b* presents the relationship between the cumulative energy dissipation and the stiffness loss. The stiffness loss represents the percentage of the initial stiffness $K_{initial}$ lost in each loading cycle. Fig. 10-*b* shows an exponential growth of the energy dissipation capacity after the specimens lose 50% of the initial stiffness. As mentioned, this limit coincides with the onset of cracking. Such behaviour indicates that, as expected, the main mechanism for energy dissipation is cracking. Initially, the energy dissipation is produced by the cracking of masonry. Once the stress transfer from the substrate to the TRM system is completed, the dissipation capacity may be also provided by the gradual damage of the basalt textile.

4.6. Damping coefficient

The equivalent viscous damping ξ_{eq} is a good indicator of the energy dissipation capacity and the stability of the hysteresis behaviour [19]. It can be computed as the ratio between the energy dissipation of the completed cycle E_d and its corresponding elastic energy E_{So} following Eq. (3).

$$\xi_{eq} = \frac{1}{4\pi}\frac{E_d}{E_{So}} \tag{3}$$

Fig. 11 shows the values of ξ_{eq} for each complete loading cycle and the corresponding stiffness loss. All the specimens showed a similar trend, in which the damping coefficient increased as damage was being accumulated. On average, up to the cracking pointing corresponding to 50% stiffness loss, the equivalent damping coefficient ξ_{eq} remained constant and with a value of almost 4%. Unlike the energy dissipation capacity, the parameter ξ_{eq} was totally independent of the damaged condition of the masonry, the presence of the reinforcement, and the failure mode. In addition, the value attained was close to the 5% proposed by EC8 [40] as the default viscous damping for the linear response analysis. After the cracking and up to 70% stiffness loss, ξ_{eq} showed a significant increase caused by the evolution of the damage. Afterwards, ξ_{eq} showed a fairly constant trend until failure. On average, this post-peak equivalent viscous damping presented a value of 11%, which is similar to the values obtained by [36] for specimens failing due to shear under cyclic testing. However, it is important to note that the equivalent viscous damping is intended to model the energy dissipation at deformation amplitudes within the linear elastic range of the overall structure. Over this range of deformations, the damping coefficient may vary with the deformation amplitude. The non-linearity observed on the damping coefficient due to increasing deformation can be handled by selecting a damping coefficient to characterise the wall associated with the linearly elastic limit of the structure. Therefore, the post-peak value of ξ_{eq} must be considered carefully since it could lead to high values which are unconservative and may not represent the real dissipation mechanism.

4.7. Drift limit state

In order to assess the behaviour of strengthened masonry walls under seismic action, it is important to identify the different levels of damage and their corresponding limit states in terms of drift values. EC8 [40] defines two main limit states to be verified in the assessment and design of URM structures. These limits correspond to Significant Damage (SD) and ultimate limit state associated with Near Collapse (NC), which are defined as a function of the failure mode. For URM walls failing in shear mode, the limit drifts corresponding to the SD and

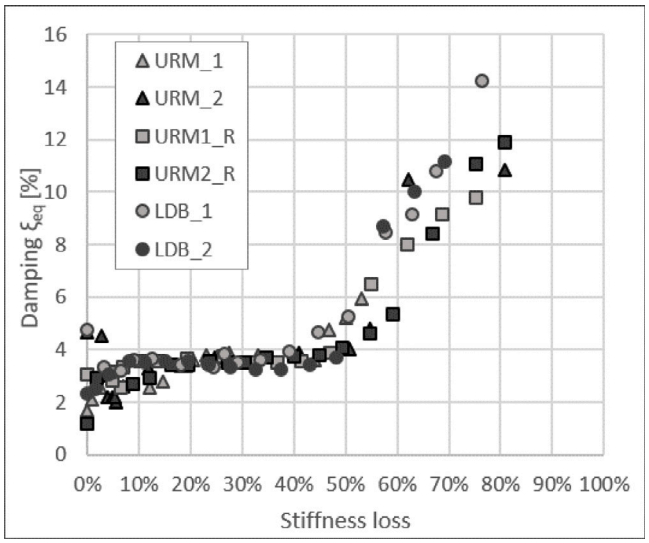

Fig. 11. Equivalent viscous damping vs. stiffness loss.

Table 3
Drift interval for the limit state proposed by CNR-DT 212 [37] according to the failure mode.

	Drift [%]		
Damage limit	DL3	DL4	DL5
Flexural failure	0.4–0.8	0.8–1.2	1.2–1.8
Shear failure	0.25–0.4	0.4–0.6	0.6–0.9

NC states are set equal to θ_{SD} = 0.4% and θ_{NC} = 0.5% respectively. The Italian standard CNR-DT 212 [37] defines three main limit states corresponding to three damage levels also as a function of the failure mode. These limits correspond to damage limit state (DL3), Significant Damage limit state (DL4), and Collapse limit state (DL5). The range of value corresponding to each limit state and failure mode are displayed in Table 3. For the sake of comparison between both standards, DL4 corresponds to SD and DL5 to NC. In the experimental curves this limit states can be identified with specific drifts. The SD limit state corresponds to the drift at the peak force, while NC limit state is associated to the post-peak drift for which the horizontal load is equal to 80% of the peak load.

It must be noted that current codes and TRM guidelines do not provide limit SD and NC drift values for strengthened walls. Using the present experimental results, an attempt is made to provide evidence on the variation of these limits in the case of B-TRM reinforced walls.

Table 4 includes the drift measurements for the previously defined limit states, SD and NC, for all specimens tested. The values were obtained by averaging the positive and the negative directions. The average values of drift experimentally obtained for the URM specimens are 0.8% and 1.1% for the SD and NC limit states respectively. When compared with the drifts limit states defined by the building codes [37,40], it is observed that both standards underestimate greatly the deformation capacity of the URM specimens. The underestimation is of about 50% and 60% for the SD and NC limit states respectively. It is important to underline that the indication of the codes is conventional and conservative, and the drift limits depend on several factors including the applied vertical load.

If the defined limit states proposed by the building codes for URM walls were applied to retrofitted walls, the drift values would be significantly underestimated as evidenced in Table 4. All retrofitted specimens showed a significant enhancement in terms of displacement capacity provided by the B-TRM strengthening, specially specimen URM2_R. However, it may be possible to explain this difference in terms of the cracking mechanisms activated during testing until the final failure of the specimen.

Table 4
Experimental drift corresponding to the limit states defined by EC8 [40].

	URM_1	URM_2	URM1_R	URM2_R	LDB_1	LDB_2
θ_{SD}	0.8%	0.9%	1.1%	1.0%	1.1%	0.9%
θ_{NC}	1.1%	1.0%	1.3%	1.6%	1.5%	1.1%

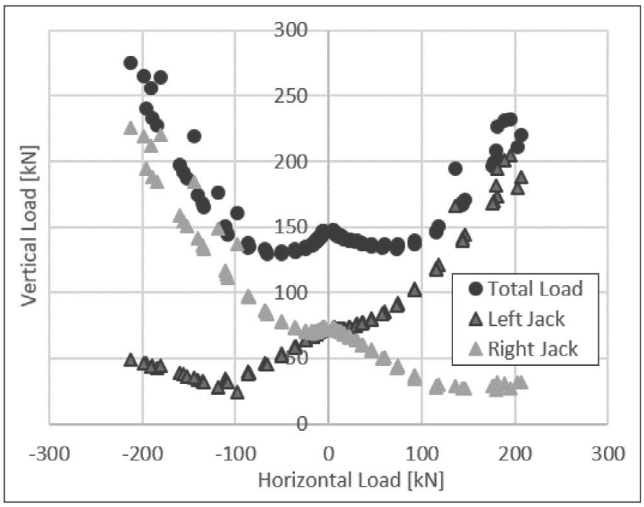

Fig. 12. Variation of the total vertical load, and the variation experienced by each jack, with increasing cyclic horizontal load.

Fig. 13-*a* shows the strength domain of the masonry wall in the σ-τ plane. In the figure, three points that represent the highlights of the test are marked. Those points are the beginning of the test, the cracking point, and the peak attainment. Those same points are represented in the force–displacement experimental curve in Fig. 13-*b*.

As mentioned in Section 3.1, the testing configuration was designed to achieve a fixed–fixed boundary condition. As a results of such configuration, with the horizontal loading the vertical load increased as consequence of the dilatancy, and thus incrementing the compressive stress experienced by the wall. This increment of the vertical load was measured by means of four pressure transducers located one on each oil chamber of the two double effect jacks that applied the vertical load in the first stage of the testing. Fig. 12 shows the vertical load variation experienced by each jack (named here as left and right, see Fig. 4) during the cyclic testing, as well as the total vertical load applied on top of the wall. The total load is obtained as the sum of the vertical loads experienced by each jack and recorded by each pressure transducer for each displacement amplitude imposed in the test.

Consequently, the σ-τ pair corresponding to the beginning of the test (represented as a square in Fig. 13) is initially located in the flexural failure of the domain. However, as the vertical load increased, and the cracking developed, the σ-τ pair moved towards the shear failure domain. Therefore, it is possible to assume that at the first stages of the test the retrofitted masonry wall experienced a flexural crack at the bottom, which due to the vertical load increment did not cause the failure of the specimen. On the contrary, such increment of the vertical load allowed the shear failure mechanism to fully develop. Therefore, the specimen may have experienced a mixed failure that provided it the ability to reach larger drift, thus explaining the significant difference in drift when compared with the standards [37,40]. Similar behaviour could be extended to the other retrofitted specimens.

Given these results, some authors [10,15] have considered the need for the definition of new limit states to understand the drift capacity of strengthened masonry.

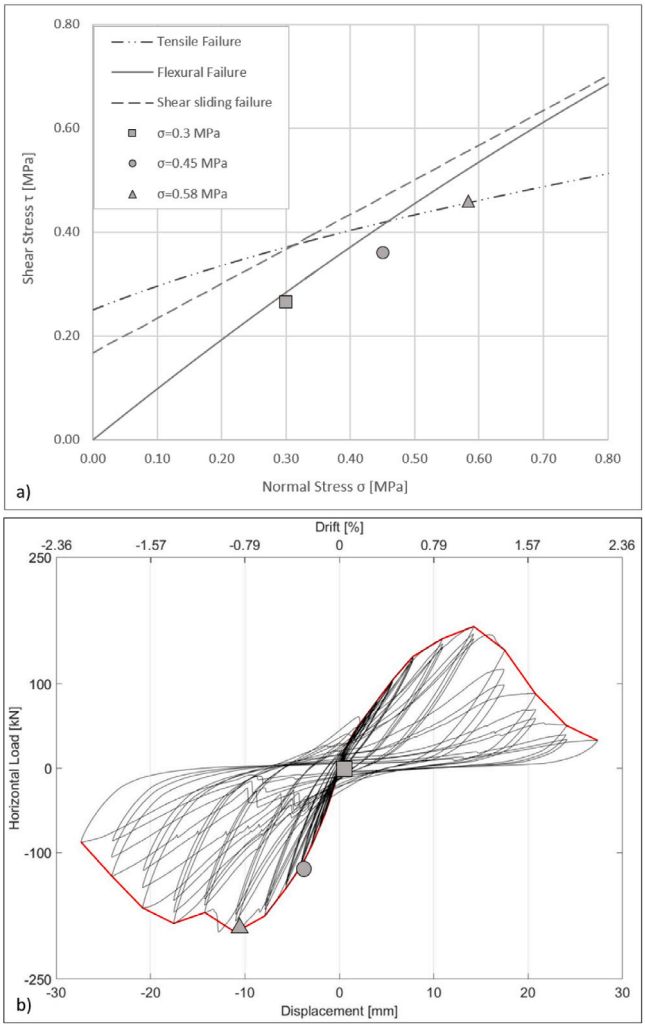

Fig. 13. (a) Strength domain of masonry wall showing three points of interest of the test: beginning of the test, cracking, peak attainment, (b) Experimental force–displacement curve of specimen URM2_R and the corresponding points of interest.

According to [41], performance-based design and assessment methods for URM structures require as input estimates the drift capacity of masonry walls. The authors also stated that better drift capacity models are required to accurately simulate the in-plane response of masonry structure. To this extent, the research presented in [10] suggested the use of additional limit states for the assessment and design of URM shear walls. First, θ_{cr} is the defined drift corresponding to the onset of cracking. Second, θ_y is defined as the drift corresponding to the yielding point of the bilinear approximation of the force–displacement response. Third, $\theta_{H_{max}}$ is the drift at the peak force, and as the one associated to the SD limit state. Fourth, θ_u is defined as the post-peak drift for which the reduction of the lateral strength is equal to 20% of the peak strength, and is associated by the building codes with the NC limit state introduced. Fifth, θ_c corresponds to the drift that triggers the global collapse and ideally relates to the full loss of the vertical load bearing capacity. The tests were stopped before the vertical residual bearing capacity vanished and therefore the true value of θ_c was not measured. As an approximation for θ_c, the drift at 50% drop of the lateral strength can be taken [10]. The defined drift limit states were computed for the present research in order to contribute to the scarce experimental database. Table 5 and Fig. 14 show the defined limit state computed for all the specimens tested.

The observed behaviour regarding the influence of the substrate damage and the failure mode is similar to that already discussed

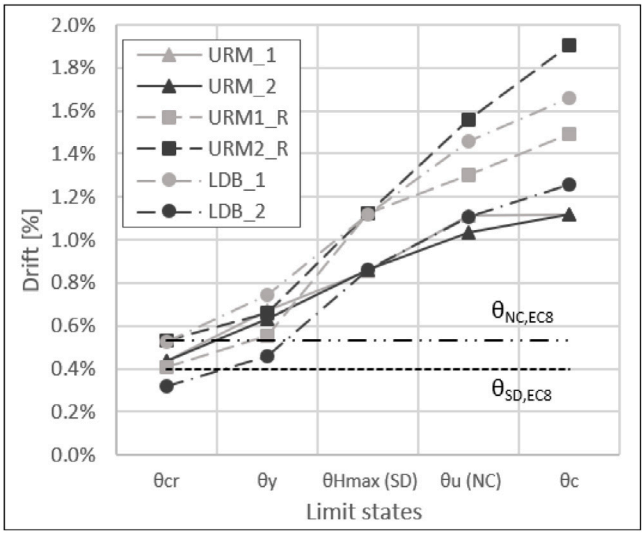

Fig. 14. Drift capacities of URM and strengthened specimens according to the limit states defined by [10] and comparison with SD and NC limit states set by EC8 [40].

with the energy dissipation. The repaired specimen URM_R attained similar values as the retrofitted specimen LDB_1 up to the drift at peak load $\theta_{H_{max}}$. After the peak load, the drift capacity of these specimens presented a broad spectrum of values. Among the retrofitted specimens, those failing in a tensile diagonal cracking (URM_R, LDB_1) showed always higher displacement capacity than the one failing due to frictional sliding (LDB_2), as evidenced in Fig. 14.

In order to validate the experimentally obtained drift capacities and provide a set of reference values for the drift capacities of retrofitted masonry, the results were compared with those of different researches involving this configuration. Table 6 shows the drift values for the limit states defined by [10] for previous experimental programmes involving SCT on retrofitted masonry. Given the limited information, not all drift limit states could be computed. In spite of the differences in masonry materials and strengthening systems, the similarity in testing methodologies and experimental results, in terms of failure modes, allows a comparative analysis. The satisfactory agreement between the values of Tables 5 and 6 reinforces the possibility of using the values of the former as reference drift limits for the design and assessment of retrofitted masonry.

5. Conclusions

The research herein presented has investigated the experimental cyclical shear behaviour of masonry walls retrofitted with B-TRM based on a continuous bidirectional grid of low density basalt (LDB). The experimental programme comprised cyclic shear compression tests on six masonry samples, two on the unreinforced configuration, two repaired and retrofitted with B-TRM, and two just retrofitted with B-TRM. The main conclusions of the research can be summarized as follows:

- Comparing the crack patterns of the URM walls with those of the retrofitted ones (URM_R, LDB), the latter experienced a more distributed damage involving both masonry and matrix. The presence of B-TRM allowed a proper redistribution of stress, and therefore, the specimens could withstand larger imposed loads and displacements, proving the efficiency of the strengthening technique.
- In the case of the URM_R specimens, the damaged condition of the substrate allowed only a moderate enhancement of the lateral load-bearing capacity, which was on average 10%, while in the case of LDB specimens the enhancement was of 30%. In spite of this difference, the increment in the displacement capacity was of about 30% for both specimen configurations.

Table 5
Experimental drifts corresponding to different damage levels according to [10].

Specimen	Cracking drift [%]	Yielding drift [%]	Maximum drift [%]	Ultimate drift [%]	Collapse drift [%]
	θ_{cr}	θ_y	$\theta_{H_{max}}$ (SD)	θ_u (NC)	θ_c
URM_1	0.4%	0.7%	0.8%	1.1%	1.1%
URM_2	0.4%	0.6%	0.9%	1.0%	1.1%
URM1_R	0.4%	0.6%	1.1%	1.3%	1.5%
URM2_R	0.5%	0.7%	1.0%	1.6%	1.9%
LDB_1	0.5%	0.7%	1.1%	1.5%	1.7%
LDB_2	0.3%	0.5%	0.9%	1.1%	1.3%

Table 6
Experimental results from previous works involving SCT on strengthened masonry walls.

References	Masonry typology	Strengthening material	Failure mode	θ_y	$\theta_{H_{max}}$	θ_u	θ_c
Gattesco et al. [42]	Rubble limestone	GFRM	DC	–	0.7%	1.1%	1.3%
Hračov et al. [43]	Clay brick	PP	DC	0.52%	0.7%	1.1%	1.2%
Torres et al. [44]	Solid ceramic brick	GTRM Repair	DC	0.1%	0.8%	1.8%	2.8%
		GTRM Retrofitting		0.1%	1.0%	1.3%	2.5%

DC: Tensile diagonal cracking, PP: Polypropylene geo-net, GFRM: Glass Fibre Reinforced Mortar, GTRM: Glass Textile Reinforced Mortar.

- The repairing technique "scuci-cuci" used on the damaged walls has allowed a full recovery of their undamaged stiffness. The initial stiffness $K_{initial}$ was marginally affected by the B-TRM due to the small thickness of the strengthening layers applied.
- The experimentally obtained effective stiffness K_e, computed as the secant stiffness at the cracking point, has agreed with the criterion of EC8 [40], according to which it can be taken as 50% of the initial stiffness $K_{initial}$. Remarkably, this criterion is also applicable to the reinforced specimens.
- As expected, the B-TRM reinforcement increased the energy dissipation capacity. However, it was also observed that the dissipation capacity was significantly influenced by the failure mode and damaged condition of the substrate. Conversely, the equivalent damping coefficient ξ_{eq} remained constant for all specimens tested, up to the cracking point. The value experimentally estimated for the damping coefficient agrees well with the one proposed by the building code EC8 [40].
- The application of the drift limit states SD and NC defined by the current building codes [37,40] has significantly underestimated the deformation capacity shown by all the tested walls. However, a mixed shear-flexural failure may explain the large difference between the experimental outcome and the drift value proposed by the building codes.

CRediT authorship contribution statement

Larisa Garcia-Ramonda: Conceptualization, Data curation, Formal analysis, Investigation, Methodology, Validation, Visualization, Writing – original draft. **Luca Pelà:** Conceptualization, Investigation, Methodology, Project administration, Validation, Funding acquisition, Supervision, Writing – review & editing. **Pere Roca:** Conceptualization, Investigation, Methodology, Project administration, Validation, Funding acquisition, Supervision, Writing – review & editing. **Guido Camata:** Conceptualization, Investigation, Methodology, Validation, Funding acquisition, Writing – review & editing.

Declaration of competing interest

The authors declare that they have no known competing financial interests or personal relationships that could have appeared to influence the work reported in this paper.

Data availability

The raw/processed data required to reproduce these findings cannot be shared at this time due to time limitations.

Acknowledgements

The authors gratefully acknowledge the financial support from the Ministry of Economy and Competitiveness and from the Ministry of Science, Innovation and Universities of the Spanish Government, as well as that of the ERDF (European Regional Development Fund) through the project SEVERUS (Multilevel evaluation of seismic vulnerability and risk mitigation of masonry buildings in resilient historical urban centres, Ref. num. RTI2018-099589-B-I00). The reinforcement systems and construction of the specimens for the experimental programme have been funded by Kerakoll Spa through the RTD project "Seismic Strengthening of Masonry Walls" (Ref. num. A-01278). The authors wish to thank Paolo Casadei, José Luis Sanchez and José Dobón from Kerakoll Spa for their involvement and support. The support from Secretaria d'Universitats i Investigació de la Generalitat de Catalunya through a predoctoral grant awarded to the first author is also gratefully acknowledged.

References

[1] Penna A, Morandi P, Rota M, Manzini CF, Da Porto F, Magenes G. Performance of masonry buildings during the emilia 2012 earthquake. Bull Earthq Eng 2014;12:2255–73. http://dx.doi.org/10.1007/s10518-013-9496-6.

[2] Valluzzi MR, Tinazzi D, Modena C. Shear behavior of masonry panels strengthened by FRP laminates. Constr Build Mater 2002;16:409–16. http://dx.doi.org/10.1016/S0950-0618(02)00043-0.

[3] Marcari G, Manfredi G, Prota A, Pecce M. In-plane shear performance of masonry panels strengthened with FRP. Composites B 2007;38:887–901. http://dx.doi.org/10.1016/j.compositesb.2006.11.004.

[4] Alecci V, Barducci S, D'Ambrisi A, De Stefano M, Focacci F, Luciano R, Penna R. Shear capacity of masonry panels repaired with composite materials: Experimental and analytical investigations. Composites B 2019;171(March):61–9. http://dx.doi.org/10.1016/j.compositesb.2019.04.013, URL https://doi.org/10.1016/j.compositesb.2019.04.013.

[5] Prota A, Marcari G, Fabbrocino G, Manfredi G. Experimental in-plane behavior of tuff masonry strengthened with cementitious matrix-grid composites. Compos Constr 2006;10:223–33. http://dx.doi.org/10.1061/(ASCE)1090-0268(2006)10.

[6] Marcari G, Basili M, Vestroni F. Experimental investigation of tuff masonry panels reinforced with surface bonded basalt textile-reinforced mortar. Composites B 2017;108:131–42. http://dx.doi.org/10.1016/j.compositesb.2016.09.094, URL http://dx.doi.org/10.1016/j.compositesb.2016.09.094.

[7] Del Zoppo M, Di Ludovico M, Balsamo A, Prota A. In-plane shear capacity of tuff masonry walls with traditional and innovative composite reinforced mortars (CRM). Constr Build Mater 2019;210:289–300. http://dx.doi.org/10.1016/j.conbuildmat.2019.03.133, URL https://doi.org/10.1016/j.conbuildmat.2019.03.133.

[8] Basili M, Vestroni F, Marcari G. Brick masonry panels strengthened with textile reinforced mortar: experimentation and numerical analysis. Constr Build Mater 2019;227. http://dx.doi.org/10.1016/j.conbuildmat.2019.117061, URL https://doi.org/10.1016/j.conbuildmat.2019.117061.

[9] Garcia-Ramonda L, Pelá L, Roca P, Camata G. In-plane shear behaviour by diagonal compression testing of brick masonry walls strengthened with basalt and steel textile reinforced mortars. Constr Build Mater 2020;240. http://dx.doi.org/10.1016/j.conbuildmat.2019.117905.
[10] Vanin F, Zaganelli D, Penna A, Beyer K. Estimates for the stiffness, strength and drift capacity of stone masonry walls based on 123 quasi-static cyclic tests reported in the literature. Bull Earthq Eng 2017;15(12):5435–79. http://dx.doi.org/10.1007/s10518-017-0188-5.
[11] da Porto F, Mosele F, Modena C. In-plane cyclic behaviour of a new reinforced masonry system: Experimental results. Eng Struct 2011;33(9):2584–96. http://dx.doi.org/10.1016/j.engstruct.2011.05.003.
[12] Akhoundi F, Vasconcelos G, Lourenço P, Silva LM, Cunha F, Fangueiro R. In-plane behavior of cavity masonry infills and strengthening with textile reinforced mortar. Eng Struct 2018;156:145–60. http://dx.doi.org/10.1016/j.engstruct.2017.11.002, URL https://doi.org/10.1016/j.engstruct.2017.11.002.
[13] Yacila J, Salsavilca J, Tarque N, Camata G. Experimental assessment of confined masonry walls retrofitted with SRG under lateral cyclic loads. Eng Struct 2019;199(April). http://dx.doi.org/10.1016/j.engstruct.2019.109555.
[14] Gattesco N, Boem I, Dudine A. Diagonal compression tests on masonry walls strengthened with a GFRP mesh reinforced mortar coating. Bull Earthq Eng 2015;13:1703–26. http://dx.doi.org/10.1007/s10518-014-9684-z, URL http://dx.doi.org/10.1007/s10518-014-9684-z.
[15] Godio M, Vanin F, Zhang S, Beyer K. Quasi-static shear-compression tests on stone masonry walls with plaster: Influence of load history and axial load ratio. Eng Struct 2019;192(May):264–78. http://dx.doi.org/10.1016/j.engstruct.2019.04.041, URL https://doi.org/10.1016/j.engstruct.2019.04.041.
[16] Bui T-l, Si Larbi A, Reboul N, Ferrier E. Shear behaviour of masonry walls strengthened by external bonded FRP and TRC. Compos Struct 2015;132:923–32. http://dx.doi.org/10.1016/j.compstruct.2015.06.057, URL http://dx.doi.org/10.1016/j.compstruct.2015.06.057.
[17] Reboul N, Mesticou Z, Si Larbi A, Ferrier E. Experimental study of the in-plane cyclic behaviour of masonry walls strengthened by composite materials. Constr Build Mater 2018;164:70–83. http://dx.doi.org/10.1016/j.conbuildmat.2017.12.215, URL http://linkinghub.elsevier.com/retrieve/pii/S095006181732620X.
[18] Papanicolaou C, Triantafillou T, Lekka M. Externally bonded grids as strengthening and seismic retrofitting materials of masonry panels. Constr Build Mater 2011;25(2):504–14. http://dx.doi.org/10.1016/j.conbuildmat.2010.07.018, URL http://dx.doi.org/10.1016/j.conbuildmat.2010.07.018.
[19] Ivorra S, Torres B, Baeza FJ, Bru D. In-plane shear cyclic behavior of windowed masonry walls reinforced with textile reinforced mortars. Eng Struct 2021;226(November 2019). http://dx.doi.org/10.1016/j.engstruct.2020.111343, URL https://doi.org/10.1016/j.engstruct.2020.111343.
[20] Mercedes L, Bernat-Maso E, Gil L. In-plane cyclic loading of masonry walls strengthened by vegetal-fabric-reinforced cementitious matrix (FRCM) composites. Eng Struct 2020;221(June). http://dx.doi.org/10.1016/j.engstruct.2020.111097, URL https://doi.org/10.1016/j.engstruct.2020.111097.
[21] Incerti A, Ferretti F, Mazzotti C. Influence of FRCM retrofitting systems on the shear behaviour of pre-damaged masonry panels. In: Milano, G. and Talercio, A. and Garrity, S. (Eds.), Proc. 10th Int. Mason. Soc. Conf. Milan; 2018. p. 2240–9.
[22] CEN. EN 772-1, Methods of test for masonry units. Part 1: Determination of compressive strength. In: Com. Eur. Norm. Brussels. 2011.
[23] CEN. EN 772-6, Methods of test for masonry units. Part 6: Determination of bending tensile strength of aggregate concrete masonry units.. In: Com. Eur. Norm. Brussels. 2002.
[24] Segura J, Aponte D, Pelà L, Roca P. Influence of recycled limestone filler additions on the mechanical behaviour of commercial premixed hydraulic lime based mortars. Constr Build Mater 2020;238. http://dx.doi.org/10.1016/j.conbuildmat.2019.117722, URL https://doi.org/10.1016/j.conbuildmat.2019.117722.
[25] CEN. EN 1015-11 - Methods of test for mortar for masonry - Part 11: Determination of flexural and compressive strength of hardened mortar. 1999.
[26] Segura J, Pelà L, Roca P. Monotonic and cyclic testing of clay brick and lime mortar masonry in compression. Constr Build Mater 2018;193:453–66. http://dx.doi.org/10.1016/j.conbuildmat.2018.10.198, URL https://doi.org/10.1016/j.conbuildmat.2018.10.198.
[27] DICAM. Relazione Tecnica sui sistemi di rinforzo Kerakoll applicati a superfici in muratura. Tech. rep., Università di Bologna - Scuola di ingegneria e architettura.
[28] Santandrea M, Imohamed I, Carloni C, Mazzotti C, de Miranda S, Ubertini F. A study of the debonding mechanism in steel and basalt FRCM masonry joints. Brick Block Mason. - Trends, Innov. Challenges 2016;433–40.
[29] Lignola GP, Caggegi C, Ceroni F, De Santis S, Krajewski P, Lourenço PB, Morganti M, Papanicolaou CC, Pellegrino C, Prota A, Zuccarino L. Performance assessment of basalt FRCM for retrofit applications on masonry. Composites B 2017;128:1–18. http://dx.doi.org/10.1016/j.compositesb.2017.05.003.
[30] Ferrara G, Caggegi C, Gabor A, Martinelli E. Experimental study on the adhesion of basalt textile reinforced mortars (TRM) to clay brick masonry: The influence of textile density. Fibers 2019;7(103). http://dx.doi.org/10.3390/fib712010.
[31] Barducci S, Alecci V, De Stefano M, Misseri G, Rovero L, Stipo G. Experimental and analytical investigations on bond behavior of basalt-FRCM systems. J Compos Constr 2020;24(1). http://dx.doi.org/10.1061/(ASCE)CC.1943-5614.0000985.
[32] Santandrea M, Daissè G, Mazzotti C, Carloni C. An investigation of the debonding mechanism between FRCM composites and a masonry substrate. Key Eng. Mater 2017;747:382–9. http://dx.doi.org/10.4028/www.scientific.net/kem.747.382.
[33] Applied Technology Council. Interim testing protocols for determining the seismic performance characteristics of structural and nonstructural components - FEMA 461. (June). 2007.
[34] Magenes G, Calvi GM. Cyclic behaviour of brick masonry walls. In: Balkema (Ed.), Proc. tenth world conf. earthq. eng. 19-24 July 1992 Madrid. Spain; 1992. p. 3517–22.
[35] Tomaževič M. Earthquake-Resistant Design of Masonry Buildings. vol. 1, Imperial Collage Press; 1999, http://dx.doi.org/10.1142/9781848160835, arXiv:arXiv:1011.1669v3, URL http://ebooks.worldscinet.com/ISBN/9781848160835/9781848160835.html,
[36] Magenes G, Calvi GM. In-plane seismic response of brick masonry walls. Earthq. Eng. Struct. Dyn. 1997;26:1091–112.
[37] CNR – Commissione di studio per la predisposizione e l'analisi di norme tecniche relative alle costruzioni. Istruzioni per la valutazione affidabilistica della sicurezza sismica di edifici esistenti CNR-DT 212/2013. 2013, p. 190.
[38] Messali F, Metelli G, Plizzari G. Experimental results on the retrofitting of hollow brick masonry walls with reinforced high performance mortar coatings. Constr Build Mater 2017;141:619–30. http://dx.doi.org/10.1016/j.conbuildmat.2017.03.112, URL http://dx.doi.org/10.1016/j.conbuildmat.2017.03.112.
[39] Knox C. Assessment of perforated unreinforced masonry walls responding in plane [Ph.D. thesis], The university of Auckland; 2012.
[40] European Standard. Eurocode 8 : Design of structures for earthquake resistance — Part 3: Assessment and retrofitting of buildings. 3, 2004.
[41] Petry S, Beyer K. Limit states of modern unreinforced clay brick masonry walls subjcted to in-plane loading. Bull Earthq Eng 2015;13:1073–95. http://dx.doi.org/10.1007/s10518-014-9695-9.
[42] Gattesco N, Amadio C, Bedon C. Experimental and numerical study on the shear behavior of stone masonry walls strengthened with GFRP reinforced mortar coating and steel-cord reinforced repointing. Eng Struct 2015;90:143–57. http://dx.doi.org/10.1016/j.engstruct.2015.02.024, URL http://dx.doi.org/10.1016/j.engstruct.2015.02.024.
[43] Hračov S, Pospíšil S, Garofano A, Urushadze S. In-plane cyclic behaviour of unfired clay and earth brick walls in both unstrengthened and strengthened conditions. Mater Struct Constr 2016;49(8):3293–308. http://dx.doi.org/10.1617/s11527-015-0720-5.
[44] Torres B, Varona FB, Baeza FJ, Bru D, Ivorra S. Study on retrofitted masonry elements under shear using digital image correlation. Sensors (Switzerland) 2020;20(7). http://dx.doi.org/10.3390/s20072122.